Equatorial Pacific Thermostad Response to El Niño

GREGORY C. JOHNSON[1*] AND ABIGAIL N. BIRNBAUM[1,2]

[1]*NOAA/Pacific Marine Environmental Laboratory, 7600 Sand Point Way NE Bldg. 3, Seattle Washington 98115, USA.*

[2]*College of Engineering, Cornell University, Carpenter Hall, Ithaca New York 14853, USA.*

for *Journal of Geophysical Research*

Submitted 2 September 2016

Revised 24 October 2016

Key Points:

- Argo temperature-salinity profile and deep velocity data are used to investigate the subsurface response of the equatorial Pacific to ENSO
- Following a moderate El Niño westward flow in the depth range of the Equatorial Intermediate Current strengthens by about 2.7 Mm^3/s
- This anomalous westward flow effects a shift of about 97 Tm^3 of Pacific Equatorial Thermostad water from the eastern to western Pacific

Abstract

El Niños are characterized by a shift of warm surface water from the western to eastern equatorial Pacific due to weakening of easterly trade winds. This shift is associated with the pycnocline (or thermocline), the large vertical density gradient beneath the surface mixed layer, shoaling in the west and deepening in the east, inducing a redistribution of ocean heat with global impacts. Here the response of the Pacific Equatorial Thermostad, a layer of low vertical stratification below the pycnocline, to El Niño is investigated using a monthly Argo float climatology and Argo float deep velocity data. A mean, seasonal cycle, trend, and time-lagged linear response to the Niño3.4 index are fit by least squares to temperature and salinity at each gridpoint as well as to deep float velocities (omitting the trend). The results of these fits are used to characterize the response of physical properties in the Thermostad, including layer thickness and velocity, to El Niño by comparing the mean properties following neutral conditions (Niño3.4 = 0 °C) versus those following a moderate El Niño (Niño3.4 = 1 °C). Following an El Niño, a strengthening of the westward-flowing Equatorial Intermediate Current of about 2.7×10^6 m^3 s^{-1} shifts about 97×10^{12} m^3 of thermostad water from the east to the west, allowing conservation of volume within the Thermostad as the pycnocline above deepens in the east and shoals in the west. This transport and volume change imply a 14-month time scale, consistent with El Niño.

1. Introduction

El Niños are associated with a large shift of warm water above the pycnocline from west to east in the equatorial Pacific [*Meinen and McPhaden*, 2000]. Because the equatorial Pacific pycnocline shoals upward from west to east, this shift of warm water also involves a very large vertical redistribution of heat that stands out in the global average [*Roemmich and Gilson*, 2011]. The redistribution is so substantial that variations in El Niños and La Niñas appear to have modulated the rate of global surface temperature rise on interannual [*Peyser et al.*, 2016] and decadal [*Kosaka and Xie*, 2013] time-scales. However, we are unaware of studies of how the layer beneath the pycnocline responds to El Niños. Here we attempt such a study of that layer, the Pacific Equatorial Thermostad (hereafter the Thermostad).

The Thermostad is a relatively vertically homogenous layer of water with temperature around 13 °C that is thickest just below the pycnocline in the eastern equatorial Pacific Ocean [*Johnson and McPhaden*, 1999; *Tsuchiya*, 1981]. The Thermostad is bounded on either side by the eastward-flowing equatorial Subsurface CounterCurrents (SCCs) or Tsuchiya Jets [*Johnson and Moore*, 1997; *Rowe et al.*, 2000; *Tsuchiya*, 1975]. It also overlaps with the westward-flowing Equatorial Intermediate Current [EIC; *Delcroix and Henin*, 1988], which is stronger in the west, the boreal fall, and El Niño [*Johnson et al.*, 2002].

The poleward migration of the SCCs has been attributed to conservation of potential vorticity following the currents; as the pycnocline shoals upward to the east, the Thermostad below gets thicker, and to conserve potential vorticity, the SCCs must move poleward where the Coriolis parameter is larger [*Johnson and Moore*, 1997]. The

meridional gradient of zonal velocity within the SCCs strengthens the potential vorticity fronts between the low values within the Thermostad and the higher values found poleward of the SCCs [*Rowe et al.*, 2000]. Since potential vorticity is conserved in inviscid flows, these strong fronts associated with the SCCs motivate using the SCCs as the poleward limits of the Thermostad.

Here we investigate how the Thermostad and currents within it respond to the change in the pycnocline associated with El Niño using a monthly gridded climatology of ocean temperature and salinity data from January 2004 through June 2016 in conjunction with Argo float 1000-dbar parking-pressure displacement data. We present the climatology, the Argo float displacement data, and a climatological index used to characterize El Niño in Section 2, our analyses of these datasets in section 3, the results of those analyses in section 4, and discussions of the results in section 5.

2. Data

We analyze a monthly gridded temperature and salinity dataset [*Roemmich and Gilson*, 2009], with a major update through 2015, and monthly updates from January through August 2016. The data are on a 1-degree latitude by 1-degree longitude grid, centered on half-degrees. The vertical coordinate is pressure, with 58 levels over from the surface to 2000 dbar. The dataset (comprising 152 consecutive months from January 2004 through August 2016) was downloaded in October 2016 from http://sio-argo.ucsd.edu/RG_Climatology.html.

We also analyze the YoMaHa'07 [*Lebedev et al.*, 2007] dataset of parking-pressure velocities derived from Argo float trajectories and provided by APDRC/IPRC. Data were downloaded from http://apdrc.soest.hawaii.edu/projects/yomaha/ on seven different dates

between June 2013 and October 2016 and then merged. We used only the data from floats with nominal parking pressures of 1000 dbar, which comprise the majority of the dataset, and span dates from July 1997 through October 2016).

As a gauge of the amplitude and phase of the El Niño Southern Oscillation (ENSO) we use the monthly Niño 3.4 index (hereafter Niño3.4), monthly sea-surface temperature anomalies within a rectangle bounded by 5ºS and 5°N in latitude and 170°W and 120°W in longitude relative to 30-year means recalculated at 5-year intervals. Niño3.4 was downloaded in October 2016 from http://www.cpc.ncep.noaa.gov/products/analysis_monitoring/ensostuff/detrend.nino34.ascii.txt.

3. Analysis

For our analysis of the Argo gridded dataset, we first use the location, in situ temperature, practical salinity, and pressure (p) values to compute, using TEOS-10 (http://www.teos-10.org/index.htm) [*IOC, SCOR, and IAPSO*, 2010], absolute salinity (S_A) and conservative temperature (Θ) at every gridpoint and time. At each gridpoint we fit, to the 152-month time-series of both S_A and Θ, by least-squares regression: a mean value, a linear temporal trend relative to the central date of the time-series, annual and semi-annual harmonics, and a three-month lagged linear response to Niño3.4. Responses to surface forcing in the sub-thermocline equatorial Pacific are typically lagged by some months [*Kessler and McCreary*, 1993; *Marin et al.*, 2010]. After removing the seasonal cycle, the maximum correlations (with magnitudes > 0.7 in some locations) between Niño3.4 and Thermostad thickness (as defined in Section 4) in the equatorial Pacific are

104 found at lags of around two months in the east and four months in the west. Hence we use
105 the average, a three-month lag, in our analysis.
106 For our analysis of the 1000-dbar Argo parking displacements, we use a modified
107 loess filter [*Cleveland and Devlin*, 1988] with a zonal scale of 10° longitude and a
108 meridional scale of 2° latitude. In addition to the conventional spatial quadratic terms and
109 the spatial weights, we add an annual harmonic, and a semi-annual harmonic following
110 *Ridgway et al.* [2002] but also adding a three-month lagged linear regression against the
111 Niño 3.4 index to match the analysis of the Argo gridded climatology. We screen any
112 trajectories that had an initial or final position over bathymetry shallower than 1050 dbar
113 to avoid including data from grounded floats. We fit velocity data at the mid-point
114 between the starting and ending location of each deep trajectory. We also discard extreme
115 outlier velocity data at each gridpoint. An extreme outlier is defined here as a value less
116 than the first quartile minus three times the interquartile range or greater than the third
117 quartile plus three times the interquartile range. The interquartile range is the range
118 between the third and first quartiles.
119 We interpret the mean values from these fits as representative of three months
120 following ENSO neutral (time-mean) conditions, and the mean values plus the Niño3.4
121 response coefficients multiplied by unity as representative of the response three months
122 following the peak of moderate (Niño3.4 = 1 °C) El Niño conditions (see Section 4). For
123 the estimated ENSO neutral and El Niño values of S_A and Θ, we further compute
124 potential density anomaly referenced to the surface (σ_0), dynamic height referenced to
125 p = 1000 dbar, and buoyancy frequency squared ($N^2 = -g/\rho\partial\rho/\partial p$), where g is the

126 acceleration of gravity and ρ is the density referenced to the central pressure over which
127 N^2 is estimated (here by vertical first-differences).
128 We use the first differences of dynamic height values to estimate zonal velocities
129 relative to zero velocity at 1000 dbar at mid-point latitudes. For the equatorial values of
130 zonal velocities we first use the meridional curvature of the dynamic heights from 1.5°S–
131 1.5°N to estimate zonal velocities over that latitude range, then multiply the results by 3
132 and subtract the off-equatorial values from 1.5–0.5°S and 0.5–1.5°N to calculate the
133 values from 0.5°S–0.5°N. We then add the 1000-dbar zonal velocities from the float
134 displacements at each location to the geostrophic zonal velocity profiles to obtain
135 estimates of absolute zonal velocities at each gridpoint.
136 We study changes of properties three months following ENSO neutral (model means)
137 and El Niño (model means + Niño3.4 coefficient, effectively three months after peak
138 Niño3.4 = 1 °C) conditions within an isopycnal layer bounding the Thermostad. We
139 choose the top boundary at σ_0 = 26.2 kg m^{-3}, near the base of the equatorial pycnocline
140 [*Johnson and McPhaden*, 1999] and the bottom boundary at 26.7 kg m^{-3}, near the base of
141 the Thermostad in the eastern equatorial Pacific [*Johnson and Moore*, 1997]. At each
142 isopycnal and geographic location for each state (following ENSO neutral and El Niño
143 conditions) we vertically interpolate values of pressure and absolute zonal velocity.

144 **4. Results**

145 The NOAA definition of an El Niño is a period when the three-month running mean
146 of Niño3.4 (Fig. 1) exceeds 0.5 °C for at least five consecutive months, and a La Niña is
147 defined as a period when that quantity falls below -0.5 °C for at least five consecutive
148 months. By these definitions there were four El Niños and three La Niñas of varying

amplitudes and durations during the time period spanned by the Roemmich and Gilson gridded Argo climatology. Niño3.4 for the time period analyzed (Fig. 1; including the three month lag) has a median value of -0.08 °C, a mean of 0.02 °C, and a standard deviation of 0.79 °C, with values ranging from -1.48 °C to +2.33 °C. Hence a typical value is near zero, with a fairly large range of values, making the regression against Niño3.4 reasonable. Defining Niño3.4 = 1 °C, which is 1.27 times the standard deviation, as equivalent to a moderate El Niño is defensible. The regressions are strongly influenced by the 2015–2016 El Niño, which has the largest variance. To put some of the El Niño responses into a temporal context, the decorrelation time-scale of the Niño3.4 over this time period, estimated as twice the integral of the lagged autocorrelation of the time-series [*Von Storch and Zwiers*, 1999], is 10 months.

The Thermostad is clearly visible as minimum in N^2 that is bounded by $26.2 < \sigma_0 < 26.7$ kg m^{-3} frequency along the equator (Fig. 2a), and within about ±5° latitude of the equator in the eastern equatorial Pacific (Fig. 2b). These bounding potential isopycnals encapsulate the Thermostad in the eastern equatorial Pacific, where it is lightest and most prominent. The Thermostad is more limited in extent and centered at higher densities in the western equatorial Pacific, as are the SCCs [*Rowe et al.*, 2000]. Here we define the poleward edges of the Thermostad layer as the poleward edges of the SCCs, where the layer-averaged velocities switch from eastward to westward, evaluated for ENSO neutral conditions. A strong potential vorticity front is located at this boundary, sharpened by the meridional gradient of zonal velocity [*Rowe et al.*, 2000].

The mean pressure of $\sigma_0 = 26.2$ kg m^{-3} (Fig. 3a), being at the base of the pycnocline [*Johnson and McPhaden*, 1999], shoals from west to east along the equator, and

generally deepens moving poleward from the equator. The slightly deeper trough of pressures at this isopycnal along the equator reflect the base of the eastward-flowing Equatorial Undercurrent (EUC), with the ridges to either side denoting the transition between the EUC and the westward flowing North and South branches of the South Equatorial Current (nSEC and sSEC). The trough in pressures along about 5°N reflects the boundary between the nSEC and the eastward flowing North Equatorial Countercurrent (NECC). The zonal ridge centered near 7°N in the western Pacific and closer to 10°N in the eastern Pacific marks the boundary between the NECC and the westward flowing North Equatorial Current (NEC).

The mean pressure of $\sigma_0 = 26.7$ kg m^{-3} (Fig. 3b) is relatively deep in a band along the equator, with shoaling rapidly to the north and south within the SSCs that form the equatorward edges of the Thermostad. This rapid shoaling occurs near ±3° latitude in the western Pacific and ±6° latitude in the eastern Pacific. There is a hint that the off-equatorial pressures are slightly greater than those on the equator, which can be seen in the meridional section at 110°W (Fig. 2b). Poleward of the SSCs, the pressures of this isopycnal increase poleward and westward.

The mean thickness between $\sigma_0 = 26.2$ and 26.7 kg m^{-3} (Fig. 3c) reflects the topography of both layers, increasing from west to east along the equator until reaching the longitude of the Galopagos Islands (~90°W), with strong thinning at about ±3° latitude in the west and ±6° latitude in the east. The thicker regions encompass the Thermostad (outlined in magenta), although including the eastward-flowing SCCs also encompasses the thin boundaries at the poleward edges of the feature.

194 Pressure on σ_0 = 26.2 kg m^{-3} is up to 30 dbar deeper following El Niño conditions
195 relative to ENSO neutral conditions in the eastern equatorial Pacific (Fig. 4a), and more
196 than 15 dbar shallower east of the Philippines. This pattern reflects the deepening of the
197 pycnocline in the east and shoaling in the west during El Niño. Pressure on
198 σ_0 = 26.7 kg m^{-3} changes exceed 5 dbar along the equator only around 105°W, but
199 deepens by as much as 15–30 dbar off the equator following El Niño relative to ENSO
200 neutral conditions, most strongly in the central equatorial Pacific (Fig. 4b). In the western
201 Pacific this isopycnal also shoals, again more strongly off the equator, with a reduction of
202 more than 20 dbar east of the Philippines and more than 10 dbar east of the Solomon
203 Islands. As a result of these changes in pressures on the Thermostad's bounding
204 isopycnals, its thickness decreases in the eastern tropical Pacific following El Niño
205 relative to ENSO neutral conditions (Fig. 4c), more so along the equator. The layer
206 thickness increases in the western tropical Pacific, especially off the equator near the
207 locations of the SCCs.
208 Mean zonal velocities near 1000 dbar from Argo profiling float deep displacement
209 data show very short (~1° lat.) meridional scale zonal jets extending across much of the
210 tropical Pacific Ocean, notably strong in the west, with a seasonal cycle that shows
211 somewhat less meridional structure [*Cravatte et al.*, 2012]. In addition, there is
212 significant seasonal and interannual variability in deep zonal velocities along the
213 equatorial Pacific evident in an earlier ALACE float data set [*Davis*, 1998]. The Niño3.4
214 regression against Argo deep displacement data suggests anomalous eastward flows
215 peaking on the equator (Fig. 5), and mostly confined to within a degree or two of it, east
216 of about 170°E following El Niño, reaching a peak of 4 cm s^{-1} around 135°W. There are

217 anomalous westward flows centered just north of the equator in the central and eastern
218 Pacific following El Niño, with a maximum exceeding 2 cm s^{-1} centered around 155°E.
219 Mean zonal geostrophic velocities referenced to mean zonal velocities at 1000 dbar
220 from Argo profiling float deep displacement data in both the western (Fig. 6a) and
221 eastern (Fig. 6b) equatorial Pacific reveal features typical of the mean circulation in these
222 locations as estimated with direct velocity measurements [*Johnson et al.*, 2002], albeit
223 somewhat broadened and smoothed. The few exceptions to this agreement are noted
224 parenthetically below.
225 In the western Pacific, at 165°E (Fig. 6a), the eastward-flowing surface-intensified
226 South Equatorial Countercurrent (SECC) is found in the upper 200 dbar, from 10°S to
227 7°S, with peak velocities exceeding 10 cm s^{-1}. From 7°S to about 1°N, the southern
228 branch of the westward-flowing, surface-intensified South Equatorial Current (sSEC) is
229 found, again mostly shallower than 200 dbar, with peak velocities exceeding 30 cm s^{-1}
230 (somewhat more than estimated from direct velocity measurements). The eastward-
231 flowing North Equatorial Countercurrent (NECC) is found from about 1°N to 8°N, with a
232 maximum in velocity reaching 20 cm s^{-1} centered at about 5°N, 90 dbar, adjoined to the
233 Equatorial Undercurrent (EUC) on its lower and southern side. North of 8°N the southern
234 edge of the North Equatorial Current (NEC) is visible. The eastward-flowing EUC has a
235 subsurface maximum exceeding 30 cm s^{-1} at around 200 dbar near the equator (slightly
236 less than estimated from direct velocity measurements). The westward-flowing
237 Equatorial Intermediate Current (EIC) is found beneath the EUC, with a peak velocity
238 exceeding 10 cm s^{-1} at about 370 dbar on the equator. The eastward-flowing northern and

239 southern Subsurface Countercurrents (nSCC and sSCC) are visible as lobes extending
240 downward and slightly poleward of the EUC, flanking the EIC at about 2°S and 3°N.
241 In the Eastern Pacific, at 110°W (Fig. 6b), the SECC is not present, the core of the
242 sSEC extends from about 7°S to 2°S, and the eastward-flowing surface-intensified
243 northern branch of the SEC (nSEC) is found from 1°S to 4°N, with a peak velocity
244 exceeding 100 cm s^{-1} (about twice estimates from direct velocity measurements). The
245 NECC is present from about 4°N to 8°N, with the southern edge of the NEC to the north
246 of the NECC. The EUC shoals with the pycnocline, with a peak velocity located at about
247 1°S and 60 dbar, all as expected, but with a peak velocity just exceeding 40 cm s^{-1} (about
248 half the peak from an estimate using direct velocity measurements). These departures
249 from expectations in the nSEC and EUC suggest that the near-surface and thermocline
250 currents may be subject to aliasing. However, the sSCC and nSCC have shifted poleward,
251 with cores at about 6°S and 6°N, as expected [*Johnson et al.*, 2002]. While the peak
252 velocities in these Thermostad-flanking currents are weaker than those in direct velocity
253 measurements (which exceed 10 cm s^{-1}), that weakness is not surprising in this relatively
254 smooth climatology.
255 Discussion of departures from ENSO neutral zonal velocities following El Niño
256 (Niño3.4 = 1 °C) are limited to the Thermostad, because the three month lag chosen is
257 best suited to that layer. In the western equatorial Pacific (at 165°E; Fig. 7a) there is
258 anomalous subsurface westward flow within most of the Thermostad, with magnitudes
259 peaking at over 10 cm s^{-1} just north of the equator. This change increases the strength of
260 the westward-flowing EIC within the Thermostad. In the eastern equatorial Pacific (at
261 110°W; Fig. 7b) zonal velocity anomalies are also generally westward within the

Thermostad, again exceeding 10 cm s^{-1} in magnitude just north of the equator near the top of the Thermostad. Within the isopycnals bounding the Thermostad, anomalous zonal velocities associated with El Niño are generally westward from around the equator, with slight eastward anomalies near the edges of the Thermostad, where the SCCs are located, suggesting an increase in the strength of these currents with El Niño. These velocity changes associated with El Niño within the Thermostad are in accord with estimates based on velocity observations from acoustic Doppler current profilers (ADCPs) [*Johnson et al.*, 2002].

Depth-integrated volume transports within the Thermostad layer (Fig. 8) are mostly westward along the equator, with smaller eastward values at the poleward edges of the layer, where the SCCs are, apparently, strengthened. These westward anomalies peak near the equator at around 110°W and 170°W, with values around -2 x 10^6 m^3 s^{-1} per degree of latitude. Thermostad layer volume changes per degree longitude (Fig. 9; blue line) increase following El Niño west of about 145°W, with peak value of about 1.6 x 10^{12} m^3 near 170°W. The Thermostad volume decreases east of about 145°W, with peak negative values of about -3.8 x 10^{12} m^3 near 95°W. The zonal volume transport anomaly within the Thermostad owing to a moderate El Niño (Fig. 9; orange line) is westward at almost all longitudes, with peak magnitudes reaching about -7.9 x 10^6 m^3 s^{-1} at around 110°W.

5. Discussion

Three months after the peak of a moderate El Niño (Niño3.4 = 1 °C), the base of the pycnocline deepens by tens of meters in the eastern equatorial Pacific and shoals by a similar amount in the western equatorial Pacific (Fig. 4a), mostly within about ±15° of

latitude of the equator. The base of the equatorial Thermostad also shoals by a similar amount in the west off the equator, and deepens in the east with smaller amplitudes than does the pycnocline, mostly within a few degrees longitude of the equator, but does not change much in depth on the equator (Fig. 4b). As a result of these changes in isopycnal pressures, the Thermostad layer thins in the eastern equatorial Pacific and thickens in the west and off the equator (Fig. 4c). The pattern of deepening isopycnals at the base of the Thermostad just off the equator (Fig. 4b) is the geostrophic signature of an anomalous westward transport within the Thermostad along the equator associated with El Niño (Figs. 7–9) — a strengthening and eastward expansion of the westward-flowing EIC.

The anomalous westward transport within the Thermostad effectively moves water west from the thinning layer east of 145°W to the thickening layer west of that longitude, conserving mass (Fig. 9). The layer thickness and zonal transport anomalies are in approximate quadrature, as might be expected for cyclic transfer in a mass-conserving system. The portion of the Thermostad that thickens with El Niño (in the western Pacific) increases in volume by 92 x 10^{12} m^3 for Niño3.4 = 1 °C and the portion that thins with El Niño (in the eastern Pacifc) decreases in volume by about 102 x 10^{12} m^3. Hence the changes in the two regions conserve mass to within about 10%. This conservation holds even neglecting the regions poleward of our definition of the Thermostad meridional boundaries, where there are some smaller changes in thickness (Fig. 4c), indicating that the Thermostad meridional boundaries of the SCCs are not actually absolute boundaries to mass transport, especially in the eastern equatorial Pacific, where meridional velocities carry El Niño signals poleward. The longitudinal average of the zonal transport anomaly associated with El Niño is about -2.7 x 10^6 m^3 s^{-1}. Dividing the average net mass change

by the average zonal transport anomaly results in a time scale of fourteen months, which is around the Niño3.4 decorrelation time scale of ten months. Using the peak transport of -7.9×10^6 m^3 s^{-1} rather than the longitudinal average yields a shorter timescale of four months.

Since this analysis is made using a linear regression, the results should scale with the Niño3.4 index, so that during a strong El Niño, the changes to isopycnal pressures, layer thicknesses, and zonal velocities will be strong. Conversely, during La Niña events the signs of these changes will be reversed. Hence, during La Niña, the pycnocline deepens in the west and shoals in the east. As a consequence, the Thermostad thickens in the east and thin in the west, with anomalous eastward flow along the equator — consistent with a weakening and contraction of the EIC. However, as noted above, the regressions are strongly influenced by the 2015–2016 El Niño, which has the largest variance.

These interannual variations in isopycnal pressures and velocities within the Thermostad could be effected primarily by Rossby waves, similar to the well-documented annual Rossby waves in the region [*Kessler and McCreary*, 1993; *Marin et al.*, 2010]. It takes a few months for the phase of these waves propagate upward and westward across the basin. The annual and semiannual harmonics fit do allow for the climatological phase propagation of the annual Rossby wave (not show). Assuming the interannual response is a modulation of the seasonal cycle [*Davis*, 1998], the simple linear regression to Niño3.4, lagged by three months, incorporates that physics to zero order.

Acknowledgments:

Argo data were collected and made freely available by the International Argo Program and the national programs that contribute to it. (http://www.argo.ucsd.edu, http://argo.jcommops.org). The Argo Program is part of the Global Ocean Observing System. Data used in this study can be accessed at the URLs found in Section 2. Comments from two anonymous reviewers greatly improved the manuscript. G.C.J. is supported by the Climate Observation Division, Climate Program Office, National Oceanic and Atmospheric Administration (NOAA), U.S. Department of Commerce and NOAA Research. A.B. was supported by the NOAA Hollings Scholar Program. Pacific Marine Environmental Laboratory Contribution Number 4556.

References

Cleveland, W. S., and S. J. Devlin (1988), Locally Weighted Regression - An Approach to Regression-Analysis by Local Fitting, *J. Am. Stat. Assoc.*, *83*(403), 596-610, doi:10.2307/2289282.

Cravatte, S., W. S. Kessler, and F. Marin (2012), Intermediate Zonal Jets in the Tropical Pacific Ocean Observed by Argo Floats, *J. Phys. Oceanogr.*, *42*(9), 1475-1485, doi:10.1175/jpo-d-11-0206.1.

Davis, R. E. (1998), Preliminary results from directly measuring middepth circulation in the tropical and South Pacific, *J. Geophys. Res.*, *103*(C11), 24619-24639, doi:10.1029/98jc01913.

Delcroix, T., and C. Henin (1988), Observations of the Equatorial Intermediate Current in the Western Pacific-Ocean (165-Degrees E), *J. Phys. Oceanogr.*, *18*(2), 363-366, doi:10.1175/1520-0485(1988)018<0363:ooteic>2.0.co;2.

IOC, SCOR, and IAPSO (2010), *The international thermodynamic equation of seawater – 2010: Calculation and use of thermodynamic properties*. Intergovernmental Oceanographic Commission, Manuals and Guides No. 56, UNESCO (English), 196 pp.

Johnson, G. C., and M. J. McPhaden (1999), Interior pycnocline flow from the subtropical to the equatorial Pacific Ocean, *J. Phys. Oceanogr.*, *29*(12), 3073-3089, doi:10.1175/1520-0485(1999)029<3073:ipffts>2.0.co;2.

Johnson, G. C., and D. W. Moore (1997), The Pacific subsurface countercurrents and an inertial model, *J. Phys. Oceanogr.*, *27*(11), 2448-2459, doi:10.1175/1520-0485(1997)027<2448:tpscaa>2.0.co;2.

362 Johnson, G. C., B. M. Sloyan, W. S. Kessler, and K. E. McTaggart (2002), Direct
363 measurements of upper ocean currents and water properties across the tropical Pacific
364 during the 1990s, *Prog. Oceanogr.*, *52*(1), 31-61, doi:10.1016/s0079-6611(02)00021-
365 6.
366 Kessler, W. S., and J. P. McCreary (1993), The annual wind-driven Rossby wave in the
367 subthermocline equatorial Pacific, *J. Phys. Oceanogr.*, *23*, 1192–1207, doi:
368 10.1175/1520-0485(1993)023<1192:TAWDRW>2.0.CO;2.
369 Kosaka, Y., and S. P. Xie (2013), Recent global-warming hiatus tied to equatorial Pacific
370 surface cooling, *Nature*, *501*(7467), 403-+, doi:10.1038/nature12534.
371 Lebedev, K., H. Yoshinari, N. A. Maximenko, and P. W. Hacker (2007), *YoMaHa'07:*
372 *Velocity data assessed from trajectories of Argo floats at parking level and at the sea*
373 *surface*, IPRC Technical Note No. 4(2), June 12, 2007, 16 pp.
374 Marin, F., E. Kestenare, T. Delcroix, F. Durand, S. Cravatte, G. Eldin, and R. Bourdallé-
375 Badie (2010), Annual reversal of the Equatorial Intermediate Current in the Pacific:
376 Observations and model diagnostics, *J. Phys. Oceanogr.*, *40*, 915–933, doi:
377 10.1175/2009JPO4318.1.
378 Meinen, C. S., and M. J. McPhaden (2000), Observations of warm water volume changes
379 in the equatorial Pacific and their relationship to El Niño and La Niña, *J. Climate*,
380 *13*(20), 3551-3559, doi:10.1175/1520-0442(2000)013<3551:oowwvc>2.0.co;2.
381 Peyser, C. E., J. Yin, F. W. Landerer, and J. E. Cole (2016), Pacific sea level rise patterns
382 and global surface temperature variability, *Geophys. Res. Lett.*, *43*,
383 doi:10.1002/2016GL069401.

384 Ridgway, K. R., J. R. Dunn, and J. L. Wilkin (2002), Ocean interpolation by four-
385 dimensional weighted least squares - application to the waters around Australasia, *J.*
386 *Atmos. Oceanic Tech.*, *19*(9), 1357-1375, doi:10.1175/1520-
387 0426(2002)019<1357:oibfdw>2.0.co;2.
388 Roemmich, D., and J. Gilson (2009), The 2004-2008 mean and annual cycle of
389 temperature, salinity, and steric height in the global ocean from the Argo Program,
390 *Progress in Oceanography*, *82*(2), 81-100, doi:10.1016/j.pocean.2009.03.004.
391 Roemmich, D., and J. Gilson (2011), The global ocean imprint of ENSO, *Geophys. Res.*
392 *Lett.*, *38*, doi:10.1029/2011gl047992.
393 Rowe, G. D., E. Firing, and G. C. Johnson (2000), Pacific equatorial subsurface
394 countercurrent velocity, transport, and potential vorticity, *J. Phys. Oceanogr.*, *30*(6),
395 1172-1187, doi:10.1175/1520-0485(2000)030<1172:pescvt>2.0.co;2.
396 Tsuchiya, M. (1975), Subsurface Countercurrents in Eastern Equatorial Pacific Ocean, *J.*
397 *Mar. Res.*, *33*, 145-175.
398 Tsuchiya, M. (1981), The Origin of the Pacific Equatorial 13-Degrees-C Water, *J. Phys.*
399 *Oceanogr.*, *11*(6), 794-812, doi:10.1175/1520-0485(1981)011<0794:tootpe>2.0.co;2.
400 von Storch, H., and F. W. Zwiers, 1999: *Statistical Analysis in Climate Research.*
401 Cambridge University Press, Cambridge, U. K., 484 pp.

Figures

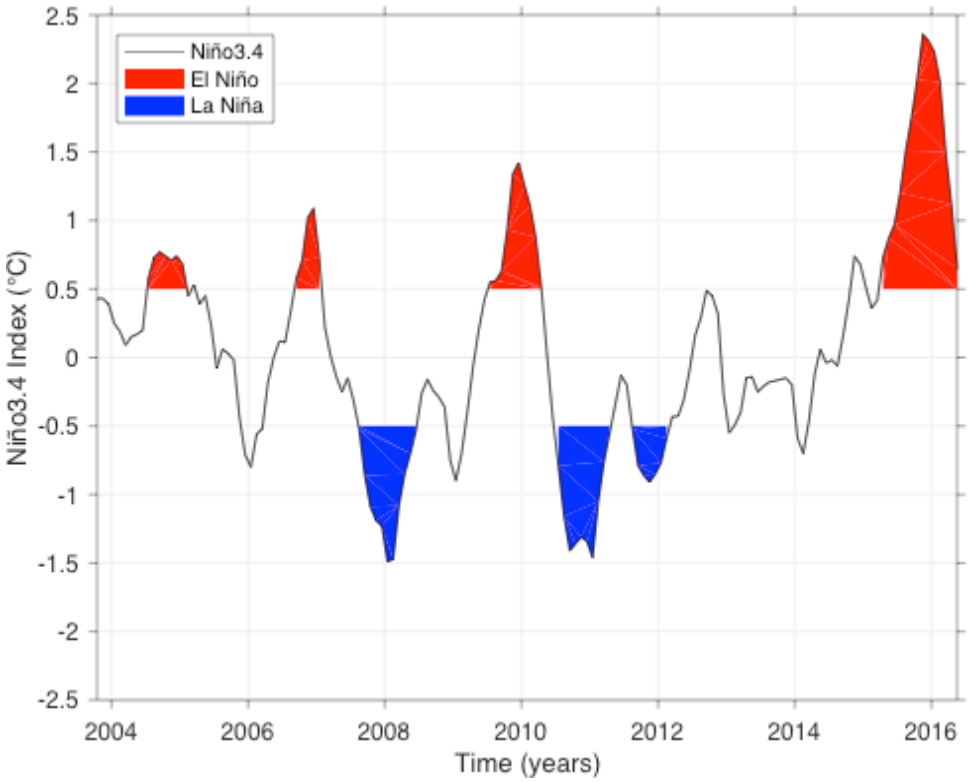

Figure 1. The Niño3.4 index (°C, black lines) for the study period with La Niña periods (blue) and El Niño periods (red) denoted (see text for definition).

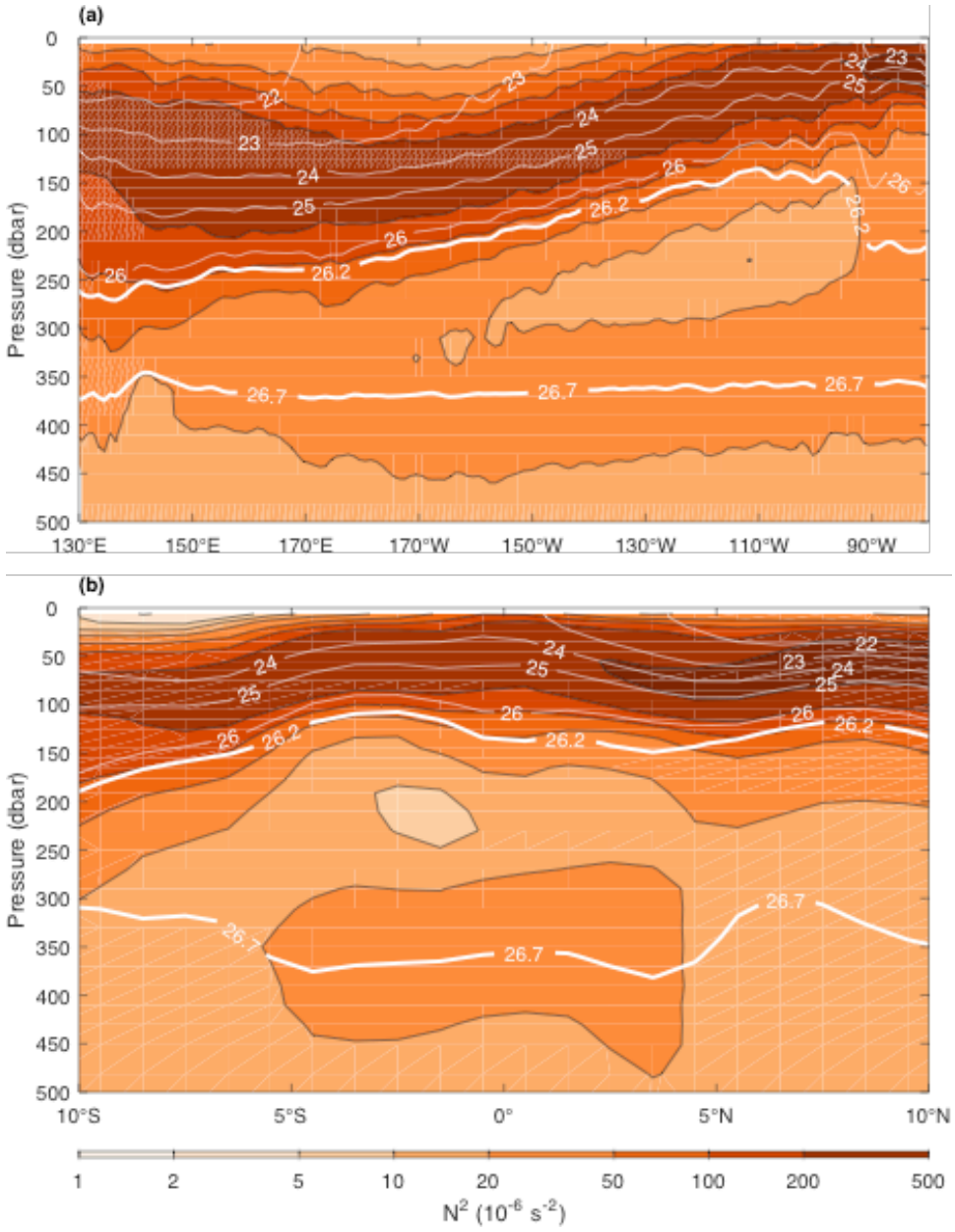

406

407 **Figure 2.** (a) Meridional-vertical section of mean buoyancy frequency squared, N^2

408 (10^{-6} s^{-2}), along the equator and (b) Zonal-vertical section of mean N^2 at 110°W. Both are

409 for ENSO neutral conditions contoured and at nearly logarithmic intervals (colorbar).

410 Potential isopycnals are contoured in white at 1 kg m^{-3} intervals (thin white lines) with

411 isopycnals bounding the Thermostad, σ_0 = 26.2 and 26.7 kg m^{-3} (thick white lines) added.

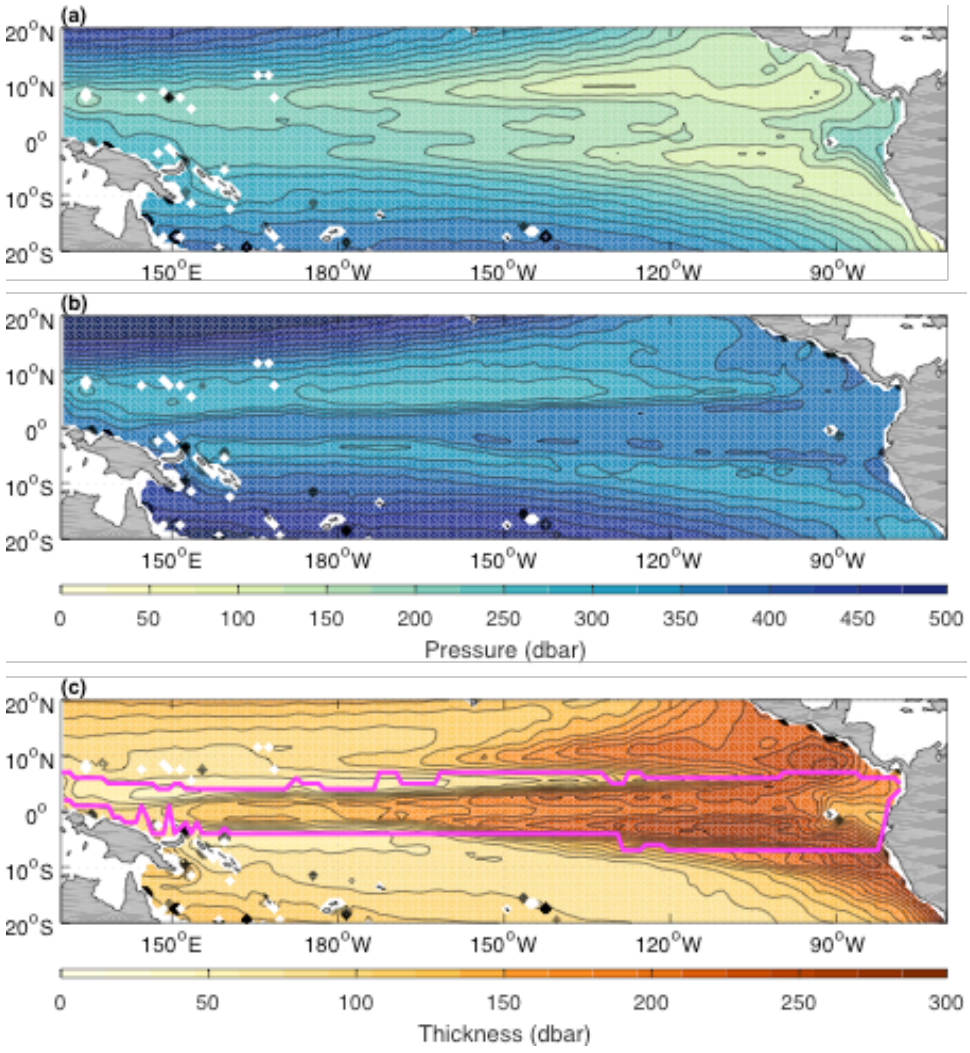

412

413 **Figure 3.** Pressure (dbar) during ENSO neutral (mean) conditions for (a)

414 σ_0 = 26.2 kg m^{-3}, (b) σ_0 = 26.7 kg m^{-3}, and (c) thickness (dbar) between σ_0 = 26.2 and

415 26.7 kg m^{-3} with Thermostad lateral boundaries (magenta lines) overplotted.

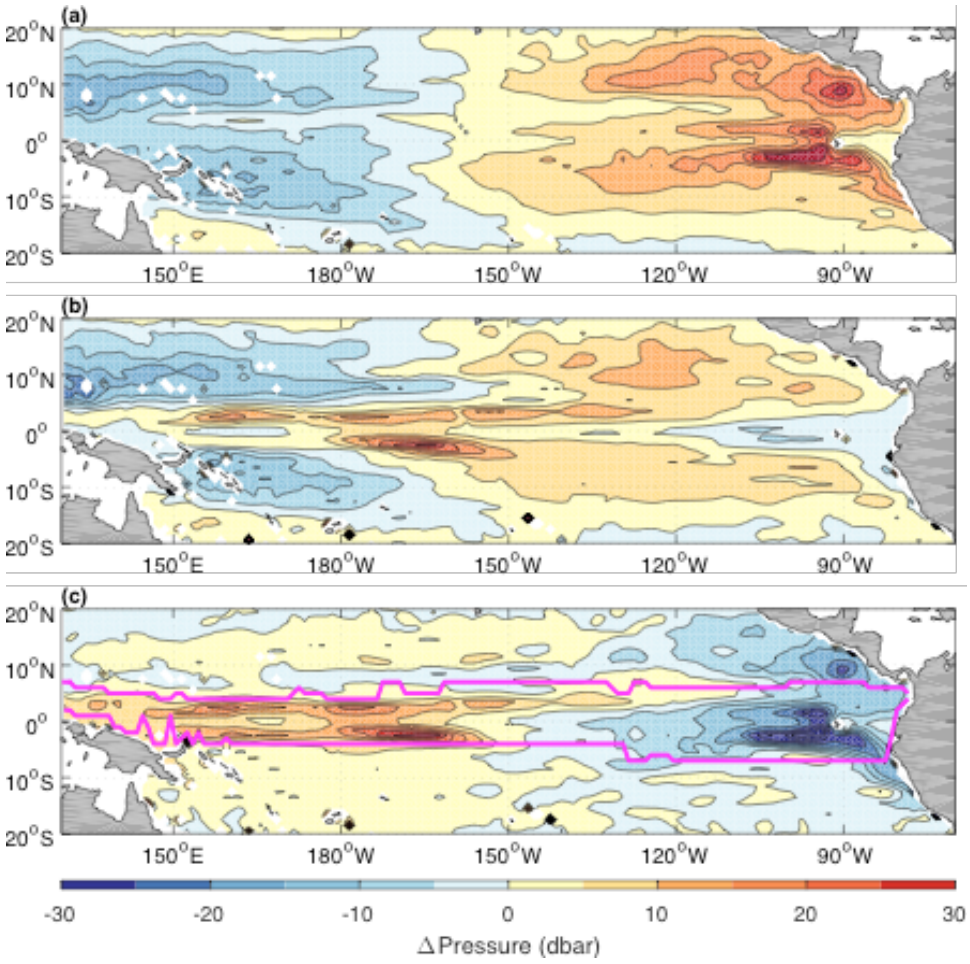

Figure 4. Pressure differences (dbar) following El Niño relative to ESNO neutral (mean) conditions for (a) pressure of σ_0 = 26.2 kg m^{-3}, (b) pressure of σ_0 = 26.7 kg m^{-3}, and (c) thickness between σ_0 = 26.2 and 26.7 kg m^{-3}, with Thermostad lateral boundaries (magenta lines) overplotted.

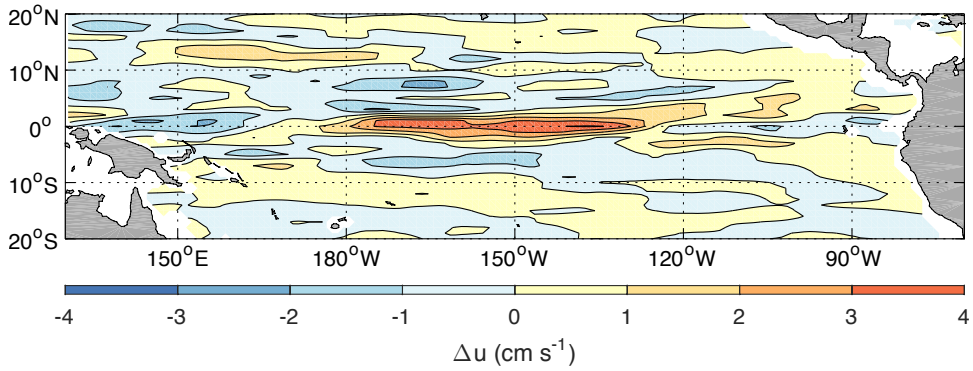

421

422 **Figure 5.** Zonal velocity difference, Δu (cm s^{-1}), following El Niño (Niño3.4 =1 °C)

423 relative to ENSO neutral (mean) conditions.

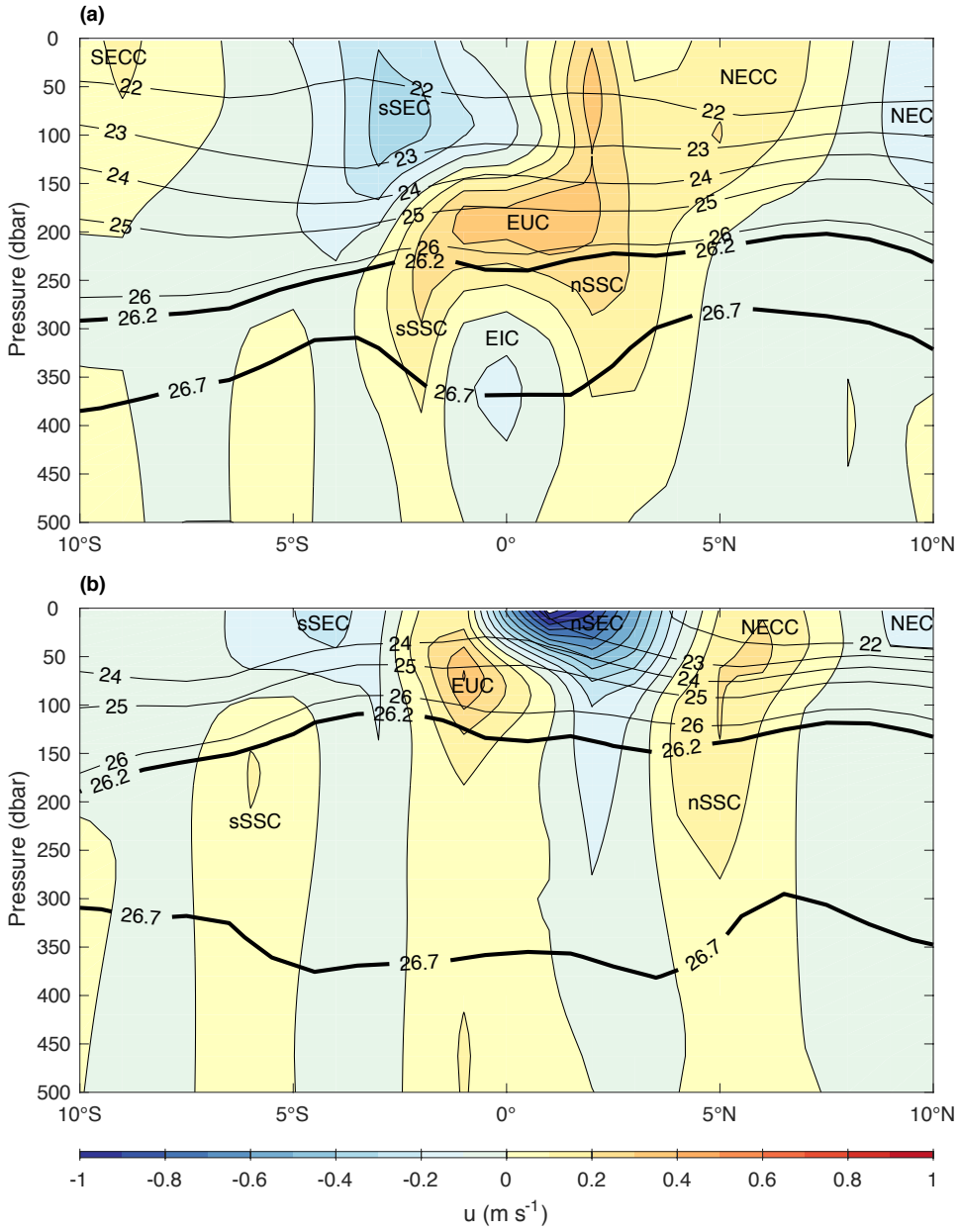

Figure 6. Meridional-vertical sections of time-mean geostrophic zonal velocity, u (m s^{-1}), referenced to 1000-dbar absolute velocities from Argo float deep displacement data for ENSO neutral conditions at (a) 165°E and (b) 110°W. Potential isopycnals contoured at 1 kg m^{-3} intervals (thin black lines) with Thermostad isopycnal boundaries (thick black lines; σ_0 = 26.2 and 26.7 kg m^{-3}) added. Locations of currents are indicated by their acronyms as defined in the text.

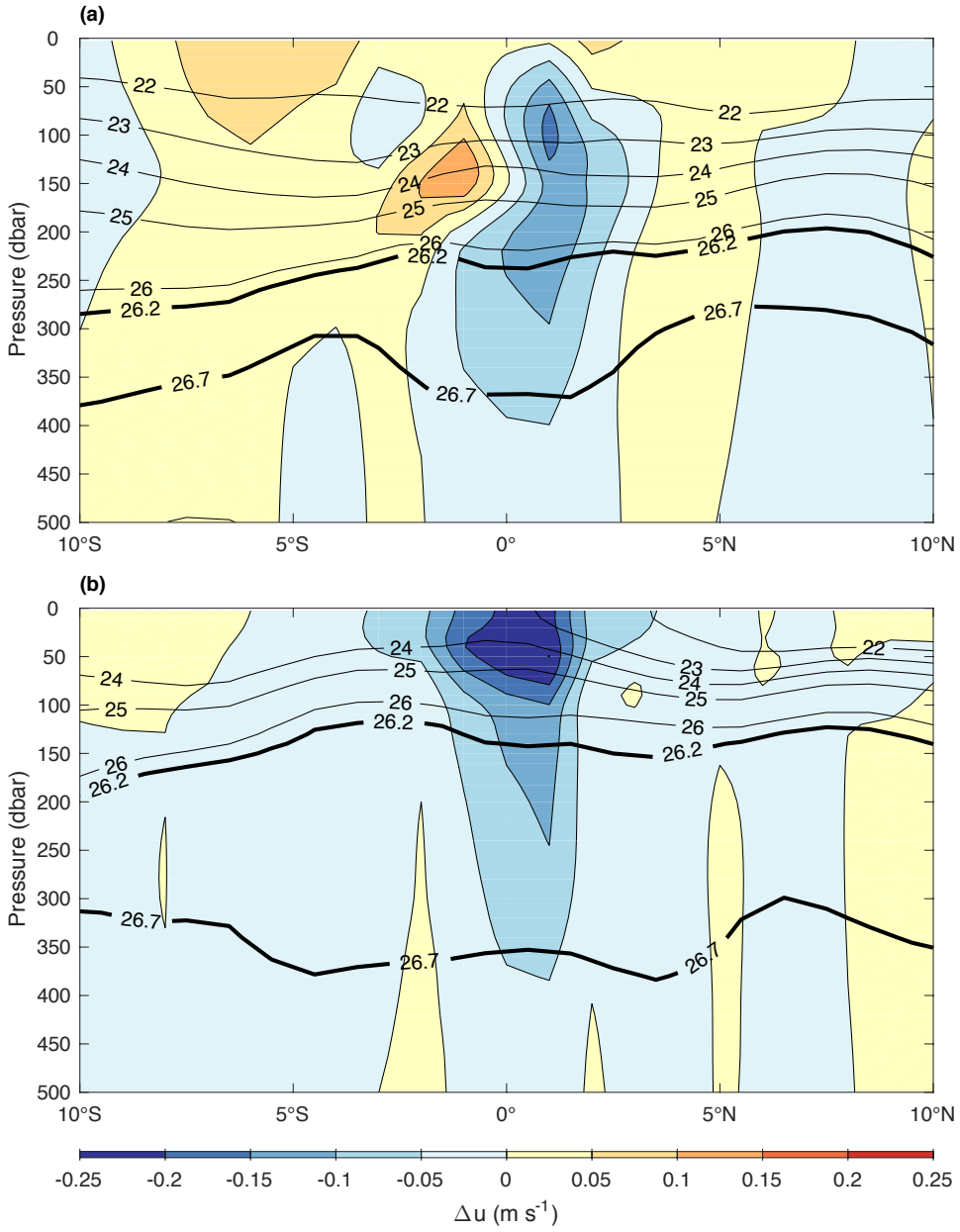

Figure 7. Meridional-vertical sections of geostrophic zonal velocity differences, Δu ($m\ s^{-1}$), following El Niño (Niño3.4 = 1 °C) relative to ENSO neutral (mean) conditions, both referenced to 1000-dbar absolute velocities from Argo float deep displacement data at (a) 165°E and (b) 110°W. Potential isopycnals contoured at 1 kg m^{-3} intervals (thin black lines) with Thermostad boundaries (thick black lines; σ_0 = 26.2 and 26.7 kg m^{-3}) added.

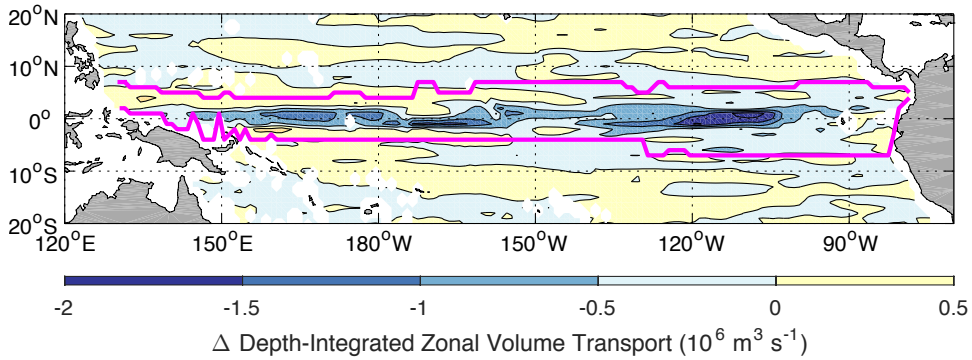

438

439 **Figure 8.** Differences of depth-integrated geostrophic zonal volume transports

440 (10^6 m^3 s^{-1}) on a 1° x 1° grid within the Thermostad isopycnal layer

441 ($26.2 < \sigma_0 < 26.7$ kg m^{-3}) following El Niño (Niño3.4 = 1 °C) relative to ENSO neutral

442 (mean) conditions with Thermostad lateral boundaries (magenta lines) overplotted.

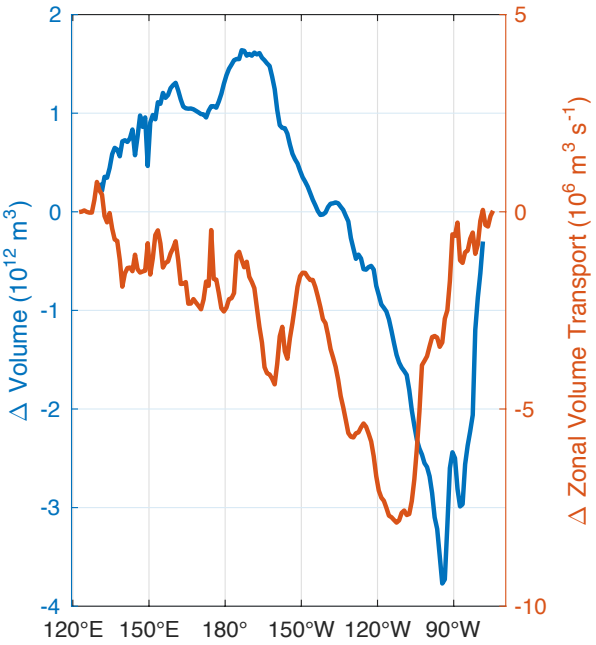

443

444 **Figure 9.** Differences of volume (blue line, 10^{12} m^3) and zonal volume transport (orange

445 line, 10^6 m^3 s^{-1}) within Thermostad isopycnal layer ($26.2 < \sigma_0 < 26.7$ kg m^{-3}) following El

446 Niño (Niño3.4 = 1 °C) relative to ENSO neutral (mean) conditions versus longitude.